



# Efficient removal of emerging organic contaminants via photo-Fenton process over micron-sized Fe-MOF sheet

Fu-Xue Wang<sup>a,b</sup>, Chong-Chen Wang<sup>a,b,\*</sup>, Xuedong Du<sup>c</sup>, Yang Li<sup>a,b</sup>, Fei Wang<sup>a,b</sup>, Peng Wang<sup>a,b</sup>

<sup>a</sup> Beijing Key Laboratory of Functional Materials for Building Structure and Environment Remediation, Beijing University of Civil Engineering and Architecture, Beijing 100044, PR China

<sup>b</sup> Beijing Energy Conservation & Sustainable Urban and Rural Development Provincial and Ministry Co-construction Collaboration Innovation Center, Beijing University of Civil Engineering and Architecture, Beijing 100044, PR China

<sup>c</sup> School of Environmental and Chemical Engineering, Yanshan University, Qinhuangdao 066004, PR China

## ARTICLE INFO

### Keywords:

Micron-sized MOF sheet

Photo-Fenton

Toxicity

Water treatment

Mechanism

## ABSTRACT

A 2D micron-sized MOF sheet, namely BUC-21(Fe), was synthesized hydrothermally from  $\text{FeSO}_4 \cdot 7\text{H}_2\text{O}$ , 1,3-dibenzyl-2-imidazolidone-4,5-dicarboxylic acid ( $\text{H}_2\text{L}$ ) and 4,4'-bipyridine (bpy), which exhibited efficient removal of chloroquine phosphate (CQ) as emerging organic pollutant model via photo-Fenton process at  $\text{pH} = 5.0$ . The generated  $\cdot\text{OH}$  concentration was  $242.5 \mu\text{mol L}^{-1}$  with  $\text{H}_2\text{O}_2$  consumption efficiency of 83.2%. The hydroxyl radical ( $\cdot\text{OH}$ ) was the primary reactive specie at the whole process, whereas superoxide radical ( $\cdot\text{O}_2^-$ ) could boost the Fenton-like reaction at neutral pH. The oxidation state and content of iron in BUC-21(Fe) was detected by X-ray absorption fine structure (XAFS), in which 62% and 45%  $\text{Fe}^{2+}$  could be observed in the fresh sample and the used sample after photo-Fenton reaction. The CQ removal efficiency decreased from 100% to 68.3% when Fe sites were locked by phosphate, directly confirming the important role of Fe in the photo-Fenton reaction. The mechanism was proposed with the help of electrochemistry and density functional theory (DFT) calculation, which revealed that the photoinduced electron was excited from oxygen atoms to Fe ions. The CQ was degraded into small molecules with low toxicity, and the degradation pathway was proposed. BUC-21(Fe) was water stable and showed excellent performance for photo-Fenton degradation of various organic contaminants (sulfamethoxazole (SMX) and bisphenol A (BPA)).

## 1. Introduction

Organic pollutants in water environment might exert great potential threat to environment due to their persistence and biotoxicity. Unfortunately, these organic pollutants, such as pharmaceutical and personal care products (PPCPs) and antibiotic, are difficult to efficiently remove via traditional process [1,2]. Advanced oxidation processes (AOPs) like photocatalysis [3–6], persulfate activation [7,8], Fenton-like and so on [9,10] have been proved to be highly efficient and eco-friendly, which are widely used in organic pollutants degradation.

Recently, increasing researchers focus on heterogeneous Fenton-like reaction for degrading organic contaminants into less toxic molecules and even mineralizing them into  $\text{CO}_2$  and  $\text{H}_2\text{O}$  [8,11]. It is expected to overcome the typical drawbacks of traditional homogeneous Fenton reaction, including but not limited to operation in the narrow pH range

(<3) and producing huge amount of sludge. However, the application of heterogeneous Fenton reaction is hampered by slow  $\text{Fe}^{2+}$  generation rate from  $\text{Fe}^{3+}$  and high  $\text{H}_2\text{O}_2$  consumption [12]. Hou et al. introduced a reductive agent  $\text{NH}_2\text{OH}$  to goethite for surface Fenton reaction, which significantly accelerated  $\text{Fe}^{2+}$  generation from  $\text{Fe}^{3+}$  [13]. Zhu et al. demonstrated that  $\text{Fe}^{3+}/\text{Fe}^{2+}$  cycle could be greatly promoted by combining ferrihydrite with carbon nanotubes (CNTs), since CNTs not only accelerated the electron transfer, but also decreased  $\text{Fe}^{3+}/\text{Fe}^{2+}$  redox potential [14]. As well, coupling technologies like photo-Fenton [15], electro-Fenton [16] and ultrasound-Fenton [17] are efficient approaches to promote  $\text{Fe}^{3+}/\text{Fe}^{2+}$  cycles and decomposition of  $\text{H}_2\text{O}_2$  [18–20]. Xing et al. demonstrated that the metal sulfide (like  $\text{MoS}_2$  [10,21] and  $\text{WS}_2$  [22]) cocatalyst greatly promoted  $\text{Fe}^{3+}/\text{Fe}^{2+}$  conversion, which resulted in high  $\text{H}_2\text{O}_2$  decomposition efficiency.

Metal-organic frameworks (MOFs) have attracted increasing

\* Corresponding author at: Beijing Key Laboratory of Functional Materials for Building Structure and Environment Remediation, Beijing University of Civil Engineering and Architecture, Beijing 100044, PR China.

E-mail address: [wangchongchen@bucea.edu.cn](mailto:wangchongchen@bucea.edu.cn) (C.-C. Wang).

<https://doi.org/10.1016/j.cej.2021.132495>

Received 17 August 2021; Received in revised form 6 September 2021; Accepted 13 September 2021

Available online 17 September 2021

1385-8947/© 2021 Elsevier B.V. All rights reserved.

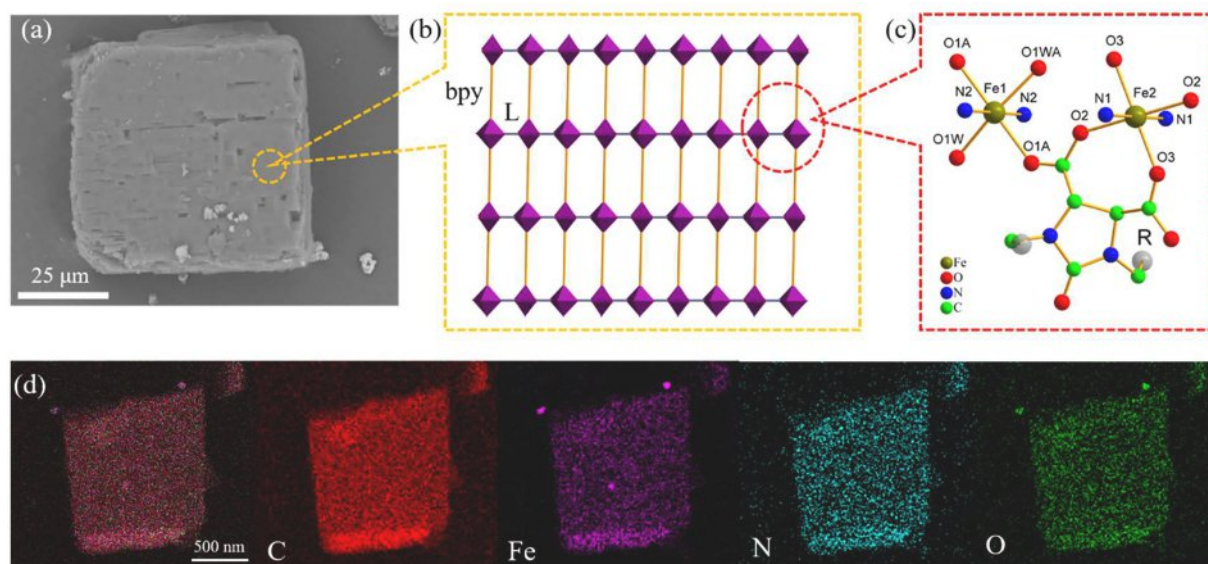


**Fig. 1.** (a) SEM image, (b) simplified crystal structure (orange sticks and gray sticks represent bpy and L, respectively), (c) coordination environment of  $\text{Fe}^{2+}$  (H atoms were omitted; R = benzyl group) and (d) EDS mappings of BUC-21(Fe) sheet.

attentions due to their diverse structures and versatile potential applications in separation [23,24], catalysis [25,26], photocatalysis [11,27], and so on [28–32]. Fe-MOFs, their composites as well as derivatives exhibited huge potential in environmental remediation, especially for heterogeneous Fenton-like reaction [33–35]. MIL-88A, a 3D Fe-MOF constructed by fumaric acid and  $\text{Fe}^{3+}$ , is considered as an eco-friendly catalyst, which have received wide interest in photo-Fenton process [36]. For example, our group demonstrated that 100% bisphenol A (BPA) was degraded over MIL-88A within 80 min under the illuminance of visible light [37], whereas the complete BPA removal could be accomplished within 30 min over polyaniline@MIL-88A composite under white light [38]. Actually, the photoinduced charges transfer rate of MIL-88A is slow because of its low conductivity. In comparison, 2D MOFs possess higher aspect ratio, more exposed activated sites, faster mass transfer rate and quicker photoinduced charges transfer rate, leading to higher photocatalytic activities [39–42]. At this point, 2D MOF nanosheets have been studied in the field of photocatalysis. Ding et al. reported in-situ growth of 2D Ni-MOF nanosheet on nickel foam (Ni-MOF/NF) without extra metal source, linked by 2-methylimidazole [43]. The as-prepared Ni-MOF/NF possessed abundant active sites and outstanding light absorption activity, which exhibited excellent photocatalytic volatile organic compounds (VOCs) degradation under visible light. Xiao et al prepared a 2D Mn-MOF (Mn-TBAPy, TBAPy = 1,3,6,8-tetrakis(*p*-benzoic acid)pyrene) nanosheet with average thickness of 9.5 nm by sonication exfoliation [44]. The  $\text{H}_2$  evolution rate on the nanosheet was 11 times higher than that on bulk Mn-MOF, which resulted from short charge transfer distance and fast charge separation on Mn-MOF nanosheet. However, the water stability of 2D MOFs nanosheets should be further concerned [45]. Accordingly, it is desired to develop 2D micron-sized MOF sheets with high catalytic activity, good water stability and low biotoxicity for environmental remediation.

Herein, a micron-sized MOF sheet, namely BUC-21(Fe), was synthesized from  $\text{Fe}^{2+}$  nodes and two ligands (1,3-dibenzyl-2-imidazolidone-4,5-dicarboxylic acid ( $\text{H}_2\text{L}$ ) and 4,4'-bipyridine (bpy)) with low toxicity (Table S1). Within this paper, chloroquine phosphate (CQ) was selected as the target emerging organic pollutant model to test the photo-Fenton performance of BUC-21(Fe). It was deemed that CQ, one of important drugs for treating malaria [46], might exert toxic effects to the non-target organisms, especially in higher pH conditions [47,48]. Within this paper, the influences of  $\text{H}_2\text{O}_2$  dosage, initial pH and co-existing inorganic anions on photo-Fenton degradation of CQ were

investigated, and the role of the surface Fe ions in the reaction was studied. The oxidation state and content of Fe were determined by X-ray absorption fine structure (XAFS). The concentration of generated  $\cdot\text{OH}$  and the  $\text{H}_2\text{O}_2$  consumption under different pH were monitored. Density functional theory (DFT) was introduced to clarify the band gap of BUC-21(Fe) and the transfer pathway of the charge carriers. As well, different organic contaminants including sulfamethoxazole (SMX) and bisphenol A (BPA) were selected to test the universality of BUC-21(Fe) as photo-Fenton catalyst for organic pollutants degradation.

## 2. Materials and methods

The information of materials, characterizations and the DFT calculation were proved in the [supplementary information](#) (SI).

### 2.1. Synthesis of BUC-21(Fe)

BUC-21(Fe) was hydrothermally synthesized similar to that of BUC-21(Zn) [49]. Briefly, a mixture of  $\text{FeSO}_4 \cdot 7\text{H}_2\text{O}$  (0.3 mmol), bpy (0.3 mmol) and  $\text{H}_2\text{L}$  (0.3 mmol) were sealed in a 25.0 mL Teflon-lined stainless steel Parr bomb containing 18.0 mL deionized water, and heated at 160 °C for 72 h. After cooling down gradually to room temperature, the as-prepared crystals of BUC-21(Fe) with the formula of  $\text{C}_{54.5}\text{H}_{45}\text{Fe}_2\text{N}_8\text{O}_{13}$  were collected by filtration.

### 2.2. Photo-Fenton catalytic experiments

Photo-Fenton CQ degradation activity of BUC-21(Fe) was investigated upon the irradiation of 10 W LED light with various wavelengths, like 365, 420, 485, 520 and 630 nm (PCX50B, Beijing Perfect Light Technology Co., Ltd), in which the corresponding light spectra were depicted in Fig. S1. The CQ residue in the aqueous solution was determined by ultra-high performance liquid chromatography (UHPLC, Thermo Scientific Vanquish Flex). The turnover frequency (TOF) was calculated by dividing the reaction rate ( $k$  value) by the catalyst concentration [34]. The products of CQ degradation were determined by LC-MS (UHPLC, Dionex UltiMate 3000 Series; MS, Q Exactive, USA). The details of photo-Fenton catalytic experiments, UHPLC and LC-MS were appended in SI.

The formed  $\cdot\text{OH}$  radicals were determined by fluorescence spectroscopy vis taking terephthalic acid (TPA) as probe. Also, the

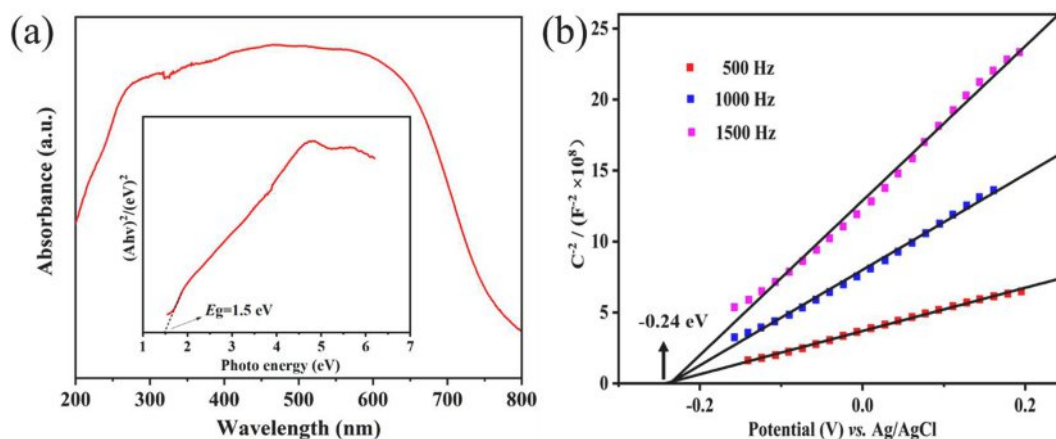


Fig. 2. (a) The UV-vis DRS,  $E_g$  plots (inset) and (b) Mott-Schottky curves of BUC-21(Fe).

concentration of generated  $\cdot\text{OH}$  radicals was qualitatively monitored at 355 nm by UHPLC. The residual  $\text{H}_2\text{O}_2$  concentration was tested by 2,9-dimethyl-1,10-phenanthroline (DMP) method [50]. Detailly, the reaction solution was added into the matrix of DMP,  $\text{CuSO}_4 \cdot 5\text{H}_2\text{O}$  and the phosphate buffer solution ( $0.1 \text{ mol L}^{-1}$ ,  $\text{pH} = 7.0$ ) to produce bright yellow complex  $\text{Cu}(\text{DMP})^{2+}$ , which was measured at 454 nm by UV-vis spectroscopy.

### 3. Results and discussion

#### 3.1. Characterizations of BUC-21(Fe)

The scanning electronic microscopy (SEM) images (Fig. 1a and Fig. S2a) demonstrated that BUC-21(Fe) displayed rough sheet

morphology with size of ca.  $60 \mu\text{m}$  length,  $60 \mu\text{m}$  width and  $5 \mu\text{m}$  thick. The single crystal structure analysis revealed that BUC-21(Fe) is constructed from  $\text{Fe}^{2+}$ ,  $\text{L}^{2-}$  and bpy (Fig. 1b). Detailly, the Fe1 was coordinated with two oxygen atoms from two different  $\text{L}^{2-}$  ligands, two oxygen atoms from two water molecules, and two nitrogen atoms from two bpy ligands (Fig. 1c), and the Fe2 was linked by four oxygen atoms from completely protonated  $\text{L}^{2-}$  and two nitrogen atoms from bpy. The detailed crystal structure data and corresponding descriptions can be found from the SI. The energy dispersive X-ray spectroscopy (EDS) elemental mapping was used to affirm the distribution of various elements (Fig. 1d), in which the uniform distribution of Fe, N (characteristic element of bpy) and O (characteristic element of  $\text{H}_2\text{L}$ ) elements could be observed. The CNHO element analyses affirmed the element of C (56.3%), N (8.9%), H (4.1%), O (19.0%) contents in the BUC-21(Fe),

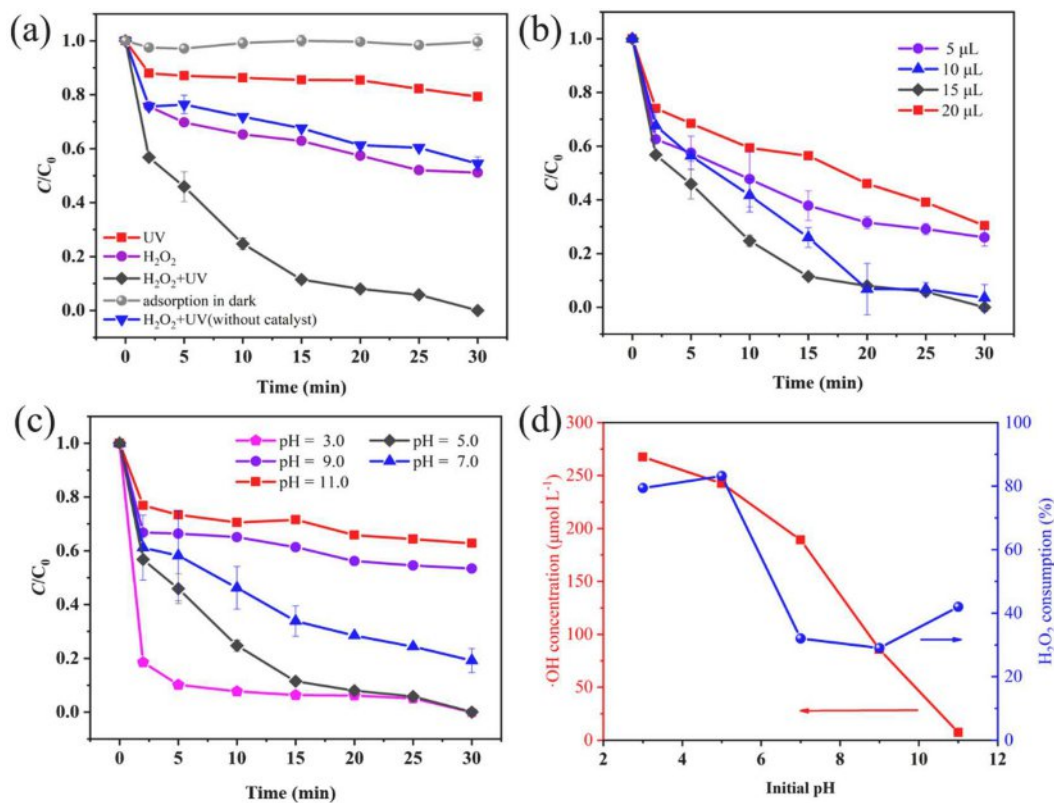


Fig. 3. (a) The CQ degradation under different conditions; (b) Photo-Fenton CQ degradation with different  $\text{H}_2\text{O}_2$  dosage (10 W LED UV light (365 nm),  $\text{pH} = 5.0$ ); (c) Effects of initial pH on photo-Fenton degradation of CQ and (d) Concentrations of  $\cdot\text{OH}$  and  $\text{H}_2\text{O}_2$  consumption at different pH values (10 W LED UV light (365 nm)). Reaction conditions: 15 mg BUC-21(Fe), 50 mL CQ ( $10 \text{ mg L}^{-1}$ ).



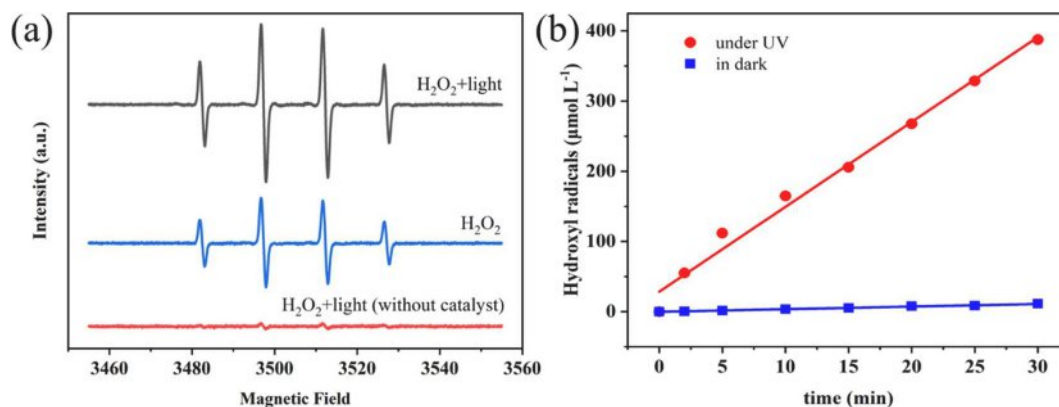


Fig. 4. (a) The ESR spectra of DMPO-·OH, (b) Concentration of ·OH radicals with time under UV light and in dark over BUC-21(Fe).

which matched well with the calculated ones based on the C<sub>54.5</sub>H<sub>45</sub>Fe<sub>2</sub>N<sub>8</sub>O<sub>13</sub> (C 57.8%, N 9.9%, H 4.0%, O 18.4%).

The powder XRD patterns (Fig. S2b) of the as-prepared BUC-21(Fe) matched well with the simulated ones from CIF file of CCDC 2,100,429 using Mercury software, suggesting the high crystallinity of as-synthesized BUC-21(Fe). FTIR spectra (Fig. S2c) indicated that the bands at 1603 and 1451 cm<sup>-1</sup> could be assigned to the asymmetric and symmetric vibration of the carboxyl group, respectively [51]. The strong characteristic peak at 702 cm<sup>-1</sup> could be ascribed to the benzene ring attached to the ligand. The peak at 482 cm<sup>-1</sup> was attributed to the Fe-O stretching vibration [52].

### 3.2. Optical property of BUC-21(Fe)

The optical performance of BUC-21(Fe) was characterized via the UV-vis DRS. It can be seen from Fig. 2a that BUC-21(Fe) could absorb a wide range of light from UV to visible light. The band gap was calculated as 1.5 eV following Eq. (1) based on UV-vis DRS data [53,54], which was close to the DFT calculated result (1.28 eV).

$$\alpha(h\nu) = A(h\nu - E_g)^2 \quad (1)$$

where  $\alpha$ ,  $h$  and  $\nu$  are the absorption coefficient, the light constant, and light frequency, respectively. The Mott-Schottky was used to determine the flat band potential of BUC-21(Fe). As illustrated in Fig. 2b, the positive slopes of Mott-Schottky plots indicated that BUC-21(Fe) is a n-type photocatalyst. Additionally, the flat band potential was -0.24 eV vs. Ag/AgCl, which was equivalent to -0.04 V vs. the normal hydrogen electrode (NHE). The lowest unoccupied molecular orbital (LUMO) potential was more negative by 0.2 V than the flat band potential [55], meaning  $E^0 = -0.24$  V (vs. NHE). Considering the effect of pH,  $E_{LUMO}$  was estimated to be -0.65 V (vs. NHE, pH = 7) following the Eq. (2) [56]. The highest occupied molecular orbital (HOMO) potential could be calculated to be 0.85 V according to the Eq. (3).

$$E_{LUMO} = E^0 - -0.05915 \times \text{pH} \quad (2)$$

$$E_{HOMO} = E_{LUMO} + E_g \quad (3)$$

### 3.3. Photo-Fenton CQ degradation performance of BUC-21(Fe)

The CQ removal efficiencies under different conditions were carried out and displayed in Fig. 3. Negligible of cationic CQ was adsorbed by BUC-21(Fe) within 30 min, which might result from low Zeta potential (Fig. S2d) and small BET specific surface area (308.87 m<sup>2</sup> g<sup>-1</sup>) of BUC-21(Fe). Besides, the 2D structure is not beneficial for adsorption, well consistent with the weak adsorption property of BUC-21(Zn) [49]. It was found that ca. 21.0% CQ was removed under UV light, indicating that BUC-21(Fe) could act as photocatalyst under light irradiation (Fig. 3a).

43.9% and 48.9% CQ was degraded in pure H<sub>2</sub>O<sub>2</sub> (H<sub>2</sub>O<sub>2</sub> + 365 nm LED UV light) and heterogenous Fenton system (BUC-21(Fe) + H<sub>2</sub>O<sub>2</sub>), respectively. In comparison, the CQ removal efficiencies were dramatically enhanced to 100% within 30 min in presence of BUC-21(Fe), H<sub>2</sub>O<sub>2</sub> and LED UV light (365 nm), which was higher than those under visible light irradiation (95.8% for 420 nm, 93.3% for 485 nm, 91.5% for 520 nm and 82.7% for 630 nm). It implied that the light, especially UV light, greatly promoted the Fenton-like reaction. From these points, it could be concluded that the effective CQ degradation could be contributed to the synergism of photocatalysis and heterogeneous Fenton-like process. Herein, the synergistic effect was determined from the degradation rates of photocatalysis ( $k_p$ ) and heterogeneous Fenton ( $k_F$ ), as disputed in Eq. (4).

$$\text{Synergy index} = \frac{k_{PF}}{k_p + k_F} \quad (4)$$

where  $k_{PF}$  was the degradation rate ( $k$  value) of photo-Fenton. The synergy index was calculated to be 5.4 (>1), implying significantly synergistic effect between photocatalysis and heterogeneous Fenton reaction.

H<sub>2</sub>O<sub>2</sub> concentration is known to influence the reaction since it can act as electron acceptor to boost the separation of photoinduced electron-hole. The photo-Fenton CQ degradation performances of BUC-21(Fe) with different H<sub>2</sub>O<sub>2</sub> dosages were investigated from 5 to 20 μL, as shown in Fig. 3b. The removal efficiencies increased from 76.3% to 100% with increasing H<sub>2</sub>O<sub>2</sub> dosage from 5 to 15 μL within 30 min, and the corresponding degradation rates ( $k$  values, Eq. (5)) increased from 0.0413 to 0.1162 min<sup>-1</sup>. However, with the further increasing dosage of H<sub>2</sub>O<sub>2</sub> to 20 μL, the degradation efficiency was reduced to 0.1101 min<sup>-1</sup>. This might be due to that the excessive H<sub>2</sub>O<sub>2</sub> could not be decomposed by photogenerated charge to yield ·OH radicals, whereas it could react with the produced ·OH radicals to form other less reactive radicals like HO<sub>2</sub>· and ·O<sub>2</sub>· (Eq. (6)) [57]. Therefore, the optimum H<sub>2</sub>O<sub>2</sub> concentration was set as 15 μL (2.94 mmol/L) for photo-Fenton CQ degradation under 365 nm LED UV light irradiation.

$$\ln(C/C_0) = -kt \quad (5)$$



The influence of initial pH on photo-Fenton CQ degradation over BUC-21(Fe) was investigated within a wide range of 3.0–11.0, as illustrated in Fig. 3c. At neutral pH (7.0), the photo-Fenton CQ degradation efficiency was 77.6% with rate of 0.0404 min<sup>-1</sup>, whereas the removal efficiency declined to 37.2% at pH = 11.0 within 30 min. In comparison, BUC-21(Fe) exhibited outstanding photo-Fenton performance at pH = 3.0, in which 81.5% CQ was removed within only 2 min. The ·OH concentration and H<sub>2</sub>O<sub>2</sub> consumption were detected at pH range of 3.0 to 11.0 (Fig. 3d). The generated ·OH was 267.5 μmol L<sup>-1</sup> with 79.4%

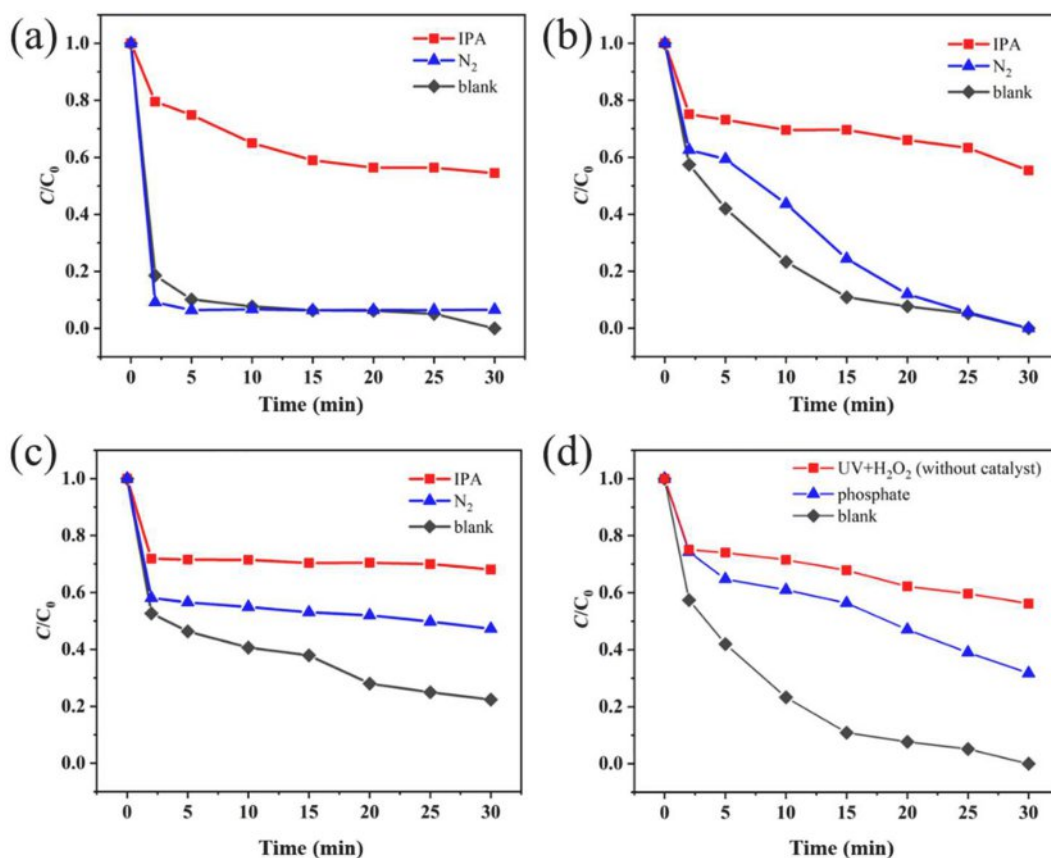


**Fig. 5.** Effect of IPA and  $N_2$  on CQ degradation over BUC-21(Fe) at (a) pH = 3.0, (b) pH = 5.0, (c) pH = 7.0 and (d) in presence of 0.2 mM phosphate, pH = 5.0. Reaction conditions: 15 mg BUC-21(Fe), 15  $\mu$ L  $H_2O_2$ , 100  $\mu$ L IPA, 50 mL CQ (10 mg  $L^{-1}$ ), 10 W LED UV light (365 nm).

$H_2O_2$  consumption at pH = 3.0, implying high  $\cdot OH$  yield and efficient utilization of  $H_2O_2$ . Besides, BUC-21(Fe) was stable under the conditions (Fig. S3). However, the  $\cdot OH$  yield decreased to only 7.3  $\mu$ mol  $L^{-1}$  at pH = 11.0 with 42.0% consumption of  $H_2O_2$ . The results directly confirmed that the low pH value was beneficial for heterogenous photo-Fenton reaction, as reported previously [58–60].

The effects of inorganic anions ( $H_2PO_4^-$ ,  $Cl^-$ ,  $HCO_3^-$ ,  $NO_3^-$  and  $SO_4^{2-}$ ) on photo-Fenton CQ degradation were carried out, in which the corresponding inorganic ions concentrations were referred from the surface water quality in Beijing [61,62]. As showed in Fig. S4, nearly 100% CQ was degraded in presence of 13.6 mg  $L^{-1}$   $NO_3^-$  and 35.0 mg  $L^{-1}$   $Cl^-$ , and small inhibition effects was observed for 19.2 mg  $L^{-1}$   $SO_4^{2-}$  and 0.85 mg  $L^{-1}$   $H_2PO_4^-$ . However, the degradation efficiency decreased to 50% when 272.0 mg  $L^{-1}$   $HCO_3^-$  was introduced into the system, in which the  $\cdot OH$  radicals might be consumed of by  $HCO_3^-$  to form  $\cdot CO_3^-$  with low oxidation potential (1.78 V) [63].

### 3.4. The identification of the reactive species

In heterogenous Fenton-like system, both  $\cdot OH$  and  $\cdot O_2^-$  radicals are usually detected. Theoretically, both the two reactive oxygen species (ROS) could be generated in photo-Fenton CQ degradation process, since the LUMO position (-0.65 V) of BUC-21(Fe) was more negative than the reduction potentials of  $H_2O_2$  ( $H_2O_2/\cdot OH$ , 0.80 V vs NHE [35]) and  $O_2$  ( $O_2/\cdot O_2^-$ ,  $E^0 = -0.18$  V [35]). Therefore, the photoexcited electron could decompose  $H_2O_2$  to form  $\cdot OH$ , as well as react with dissolved oxygen (DO) to yield  $\cdot O_2^-$ . The ESR was adopted to detect active radicals, in which dimethyl pyridine N-oxide (DMPO) was used to capture  $\cdot OH$  and  $\cdot O_2^-$ . As displayed in Fig. 4a, weak DMPO- $\cdot OH$  could be found in “ $H_2O_2$  + light” system, suggesting  $H_2O_2$  could be decomposed by light to yield  $\cdot OH$ . Obvious signals emerged in “BUC-21(Fe) +  $H_2O_2$ ”

system, whereas the signals were further promoted under UV light irradiation. This was because that BUC-21(Fe) could decompose  $H_2O_2$  to generate  $\cdot OH$  radicals under dark condition, which was greatly accelerated under UV light. Additionally, the DMPO- $\cdot O_2^-$  signals could be found during photocatalytic process (Fig. S5). It is generally deemed that  $\cdot OH$  can be trapped by TPA to form 2-hydroxy terephthalic acid, which can be excited at 315 nm to emit fluorescence at 425 nm [64]. The fluorescence method was used to determine the generated  $\cdot OH$ . As showed in Fig. S6, it could be found that the signals became increasingly obvious with time, implying that the  $\cdot OH$  concentration increased rapidly. The  $\cdot OH$  radicals can react with dimethyl sulfoxide (DMSO) to quantitatively yield formaldehyde. The 2,4-dinitrophenylhydrazine (DNPH) can further react with the formed formaldehyde in  $K_2HPO_4$ - $KH_2PO_4$  buffer solution (pH = 4.0) to produce hydrazone compound (DNPHo), which is stable and can be determined by UHPLC [65]. The  $\cdot OH$  concentration in the photo-Fenton reaction was determined to reach 242.5  $\mu$ mol  $L^{-1}$  within 30 min, whereas it was only 11.3  $\mu$ mol  $L^{-1}$  in dark condition (Fig. 4b), suggesting that the UV light significantly promoted  $\cdot OH$  generation.

However, the contribution of the two radicals to the heterogenous photo-Fenton reaction under different pH is unclear. To clarify the contribution of  $\cdot OH$  and  $\cdot O_2^-$  on photo-Fenton CQ degradation, the isopropyl alcohol (IPA) was added as  $\cdot OH$  scavenger and the  $N_2$  gas was bubbled to remove the DO to inhibit the formation of  $\cdot O_2^-$  radicals. The degradation efficiencies were obviously inhibited in presence of IPA from pH 3.0 to 7.0. Under acid conditions (pH  $\leq$  5.0), the influence of bubbling  $N_2$  gas on CQ degradation were negligible (Fig. 5a and 5b), demonstrating that  $\cdot OH$  rather than  $\cdot O_2^-$  was the main ROS. Under the condition of pH = 7.0 (Fig. 5c), the CQ removal efficiency decreased by 45.7% and 24.9% after adding IPA and bubbling  $N_2$  gas, respectively. It implied that both  $\cdot OH$  and  $\cdot O_2^-$  contributed to the photo-Fenton

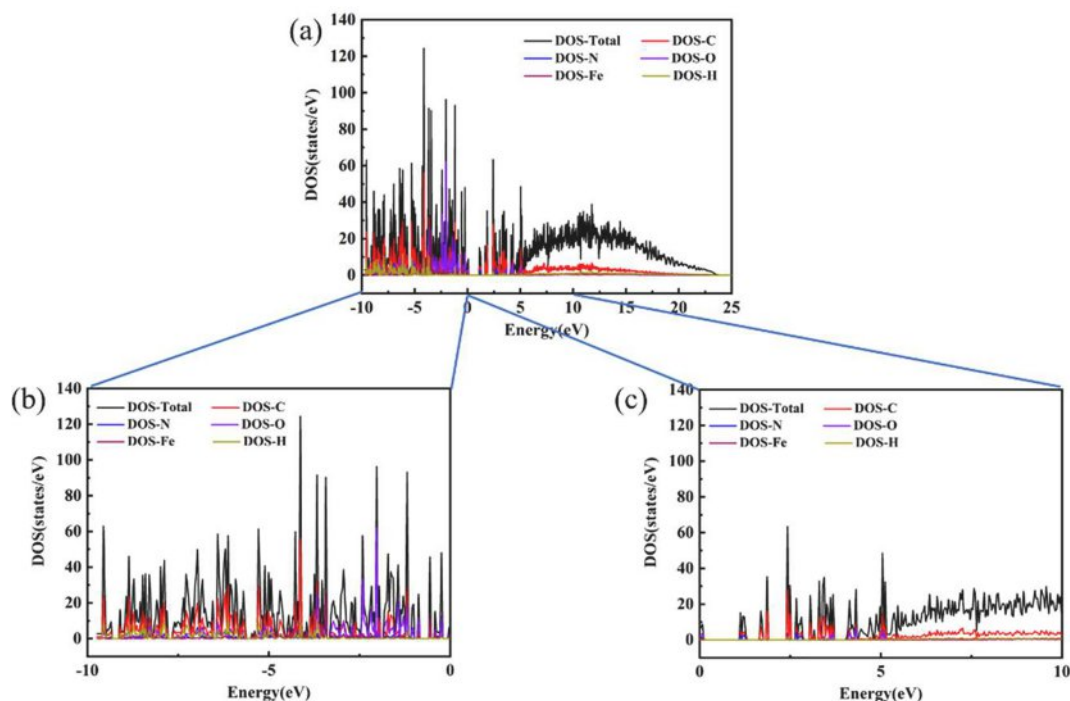


Fig. 6. (a) Total density of states (TDOS) and (b-c) partial density of states (PDOS) projected onto different atomic orbitals. The Fermi level was set to 0.

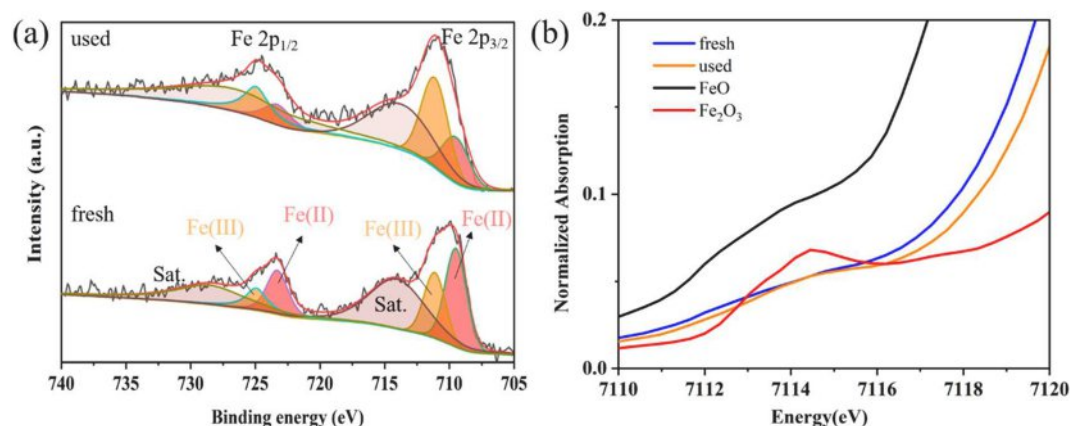


Fig. 7. (a) XPS and (b) Fe K-edge (pre-edge) XANES spectra of BUC-21(Fe) before and after photo-Fenton reaction.

reaction at pH = 7.0, in which  $\cdot\text{OH}$  played a more important role in the process.

Previously, Hou et al. detected the contribution of surface  $\text{Fe}^{2+}$  on the catalyst by chelating them with 1,10-phenanthroline or bipyridine during heterogeneous Fenton reaction [13]. As well, the phosphate ions can react with Fe sites and inhibited the activity of catalysts. Yu et al. blocked the surface Fe sites with phosphate in catalytic ozonation, in which the 4-nitrophenol removal efficiency decreased from 100% to 41.4% [66]. Yang et al. demonstrated that the formed iron phosphate precipitated on the surface of the catalyst, which hampered  $\text{H}_2\text{O}_2$  decomposition and decreased heterogeneous Fenton oxidation of catechol [67]. In order to determine the contribution of the surface Fe sites in photo-Fenton CQ degradation, phosphate was introduced into the reaction system. As illustrated in Fig. 4d, the CQ removal efficiency decreased from 100% to 68.3% when  $0.2 \text{ mmol L}^{-1}$  phosphate was added into the photo-Fenton system. As well, the consumed  $\text{H}_2\text{O}_2$  decreased from 83.2% to 39.1%. The results suggested the important role of Fe sites in heterogeneous photo-Fenton process.

### 3.5. Photo-Fenton catalytic mechanism

The transportation of photoinduced electron was identified by analyzing the electronic density distribution (Bader Charge) and density of (electronic) states (DOS) of BUC-21(Fe). As illustrated in Fig. 6, the energy levels in the range of  $-4.5$  to  $-3.0$  eV were mainly formed by C-1s state and a small amount of Fe-2p state, whereas the HOMO (VB) in the range of  $-2.5$  to  $0$  eV was mainly coupled from O-2p state, suggesting that oxygen atoms supplied electrons to the heterogeneous photo-Fenton reaction. There was hardly N-1s state in the range of  $-4.5$  to  $0$  eV, indicating it played a negligible role in the redox reaction. Moreover, the energy levels in the range of  $0$  to  $5.0$  eV were mainly filled with the electrons of carbon and oxygen atoms. Besides, the results of Bader Charge listed in Table S4 were consistent with the propose that the charge transfer from oxygen atoms to Fe ions.

The XPS spectrum of Fe 2p for BUC-21(Fe) is described in Fig. 7a. The binding energies of Fe  $2p_{3/2}$  and Fe  $2p_{1/2}$  are 710.0 and 723.2 eV, respectively. The fitting peaks at 709.3 and 723.6 eV are assigned to  $\text{Fe}^{2+} 2p_{3/2}$  and  $\text{Fe}^{2+} 2p_{1/2}$ , respectively. The binding energy difference

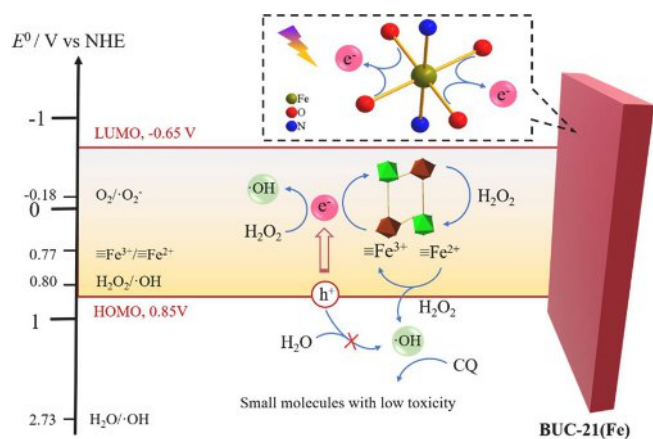


Fig. 8. Plausible mechanism of photo-Fenton degradation CQ over BUC-21(Fe) sheet.

between the Fe  $2p_{3/2}$  peak and the satellite peak (714.9 eV) is 4.9 eV, close to the difference (5.3 eV) of  $\text{FeSO}_4$  reported previously [68]. After photo-Fenton reaction, the intensity of  $\text{Fe}^{2+}$  decreases obviously, while no substantial change could be found on binding energy. However, the peaks at 711.5 and 725.2 eV may result from the existence of  $\text{Fe}^{3+}$ , which attribute to  $\text{Fe}^{3+} 2p_{3/2}$  and  $\text{Fe}^{3+} 2p_{1/2}$ , respectively [35,69].

Furthermore, in order to clarify the oxidation states and the corresponding content of each Fe-form in the catalyst before and after photo-Fenton reaction, linear combination of Fe K-edge X-ray absorption near edge structure (XANES) spectra of BUC-21(Fe) was fitted to those of as-received FeO ( $\text{Fe}^{2+}$ ) and  $\text{Fe}_2\text{O}_3$  ( $\text{Fe}^{3+}$ ), respectively. The  $\text{Fe}^{2+}$  pre-edge at ca. 7112 eV represents the 1s to 3d transition, whereas the pre-edge peak for  $\text{Fe}^{3+}$  is at 7114 eV, since the electrons are more strongly bound to the Fe nucleus than that to  $\text{Fe}^{2+}$ , resulting in a shift towards high energy [70]. As showed in Fig. 7b and Fig. S7, the fresh BUC-21(Fe) sample demonstrated the peak with binding energy of 7112 eV, similar

with that of standard iron oxide ( $\text{Fe}^{2+}$ ), suggesting that the oxidation state of Fe in BUC-21(Fe) is + 2. However, the Fe K edge of the used sample shifted to a higher binding energy, implying that the oxidation state of Fe became higher after photo-Fenton reaction. This might result from oxidation of  $\text{Fe}^{2+}$  by  $\text{H}_2\text{O}_2$  to form  $\text{Fe}^{3+}$ . The fitting results, illustrated in Table S5, included the identified components, content and residual factor for each fit, in which the  $\text{Fe}^{2+}$  content on the surface of the fresh BUC-21(Fe) sample was calculated as 62%. After heterogeneous photo-Fenton reaction, the  $\text{Fe}^{2+}$  content decreased to 45%, further confirming that the heterogeneous Fenton-like process occurred on the surface of the BUC-21(Fe) sheet.

In the Fenton-like reaction, the Fe ion may unavoidably be leached to the solution and accomplishes homogeneous Fenton reaction. Herein, the leaching Fe from BUC-21(Fe) was only  $1.5 \text{ mg L}^{-1}$  (5.05% of Fe) during the whole photo-Fenton reaction, suggesting that the surface Fe ( $\equiv\text{Fe}$ ) was the main activity sites for decomposing  $\text{H}_2\text{O}_2$ . Based on the above results, a possible mechanism for photo-Fenton degradation of CQ over BUC-21(Fe) was proposed (Fig. 8). Under UV light irradiation, electrons ( $e^-$ ) and holes ( $h^+$ ) were excited to produce at the HOMO and LUMO of BUC-21(Fe), as Eq. (4). The  $e^-$  could not only decompose  $\text{H}_2\text{O}_2$  to yield  $\cdot\text{OH}$ , but also reduce  $\equiv\text{Fe}^{3+}$  to  $\equiv\text{Fe}^{2+}$  ( $\text{Fe}^{3+}/\text{Fe}^{2+}$ ,  $E^0 = 0.77 \text{ V vs NHE}$  [71]) (Eq. (7)–(9)), which efficiently prevented the recombination of  $e^- - h^+$  pairs. The linear sweep voltammetry (LSV) was adopted to confirm the role of  $\text{H}_2\text{O}_2$  in electron transfer. As illustrated in Fig. S8, the addition of  $\text{H}_2\text{O}_2$  significantly enhanced the current response, indicating that the redox reaction between  $\text{H}_2\text{O}_2$  and BUC-21(Fe) was enhanced for the fast electron transfer process. Similar phenomenon could be found in metal-free catalyst like swine manure biochar [72]. In addition, partial  $e^-$  could react with DO to produce  $\cdot\text{O}_2^-$  (Eq. (10)). Whereas, the  $h^+$  cannot oxidize  $\text{H}_2\text{O}$  to yield  $\cdot\text{OH}$  since the oxidation potential of  $\text{H}_2\text{O}$  ( $E^0 = 2.73 \text{ V vs NHE}$  [35]) was much more positive than that of the HOMO of BUC-21(Fe) (0.85 V). The  $\equiv\text{Fe}^{2+}$  could directly decompose  $\text{H}_2\text{O}_2$  to yield  $\cdot\text{OH}$  (Eq. (11)) and to produce  $\equiv\text{Fe}^{3+}$ , which could also be reduced to  $\equiv\text{Fe}^{2+}$  by  $\text{H}_2\text{O}_2$  (Eq. (12)). It was deemed that  $\equiv\text{Fe}^{3+}/\equiv\text{Fe}^{2+}$  cycles were promoted by both of photogenerated electron and  $\text{H}_2\text{O}_2$ . Similar result can be found in photoelectron-Fenton reaction process [35].

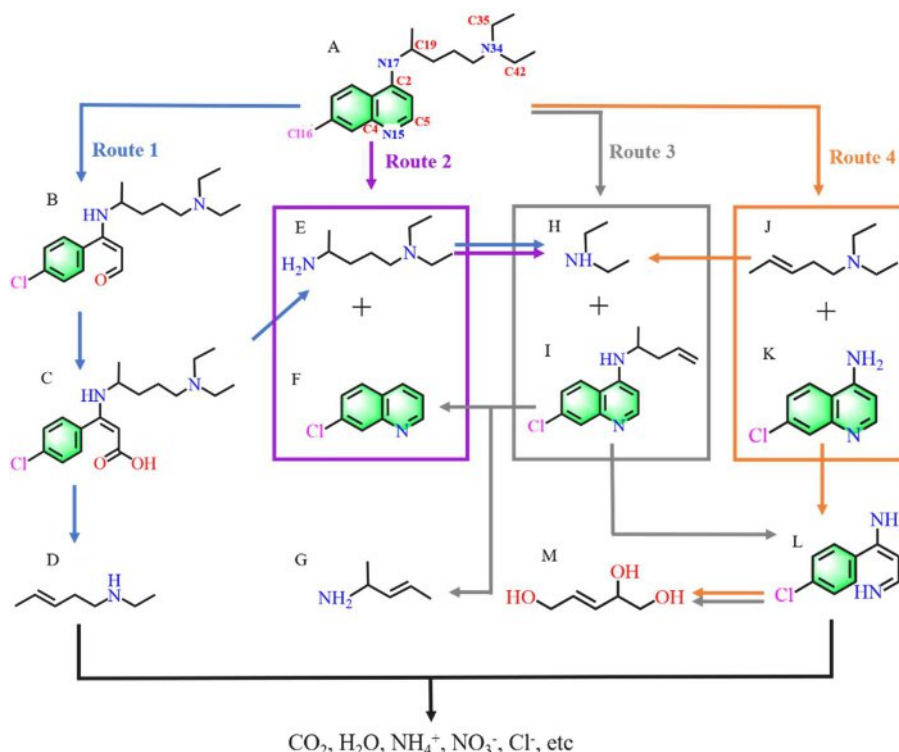


Fig. 9. Photo-Fenton degradation pathway of CQ over BUC-21(Fe).



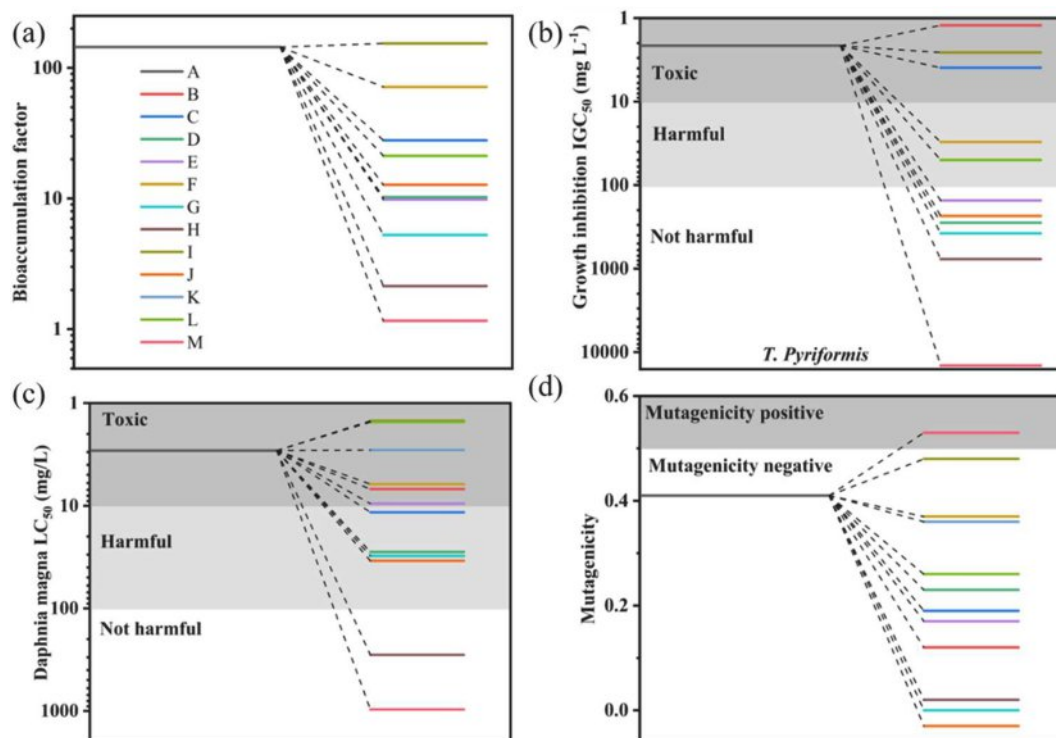


Fig. 10. (a) Bioaccumulation factor, (b) growth inhibition, (c) Daphnia magna  $LC_{50}$  and (d) mutagenicity of CQ and intermediates.

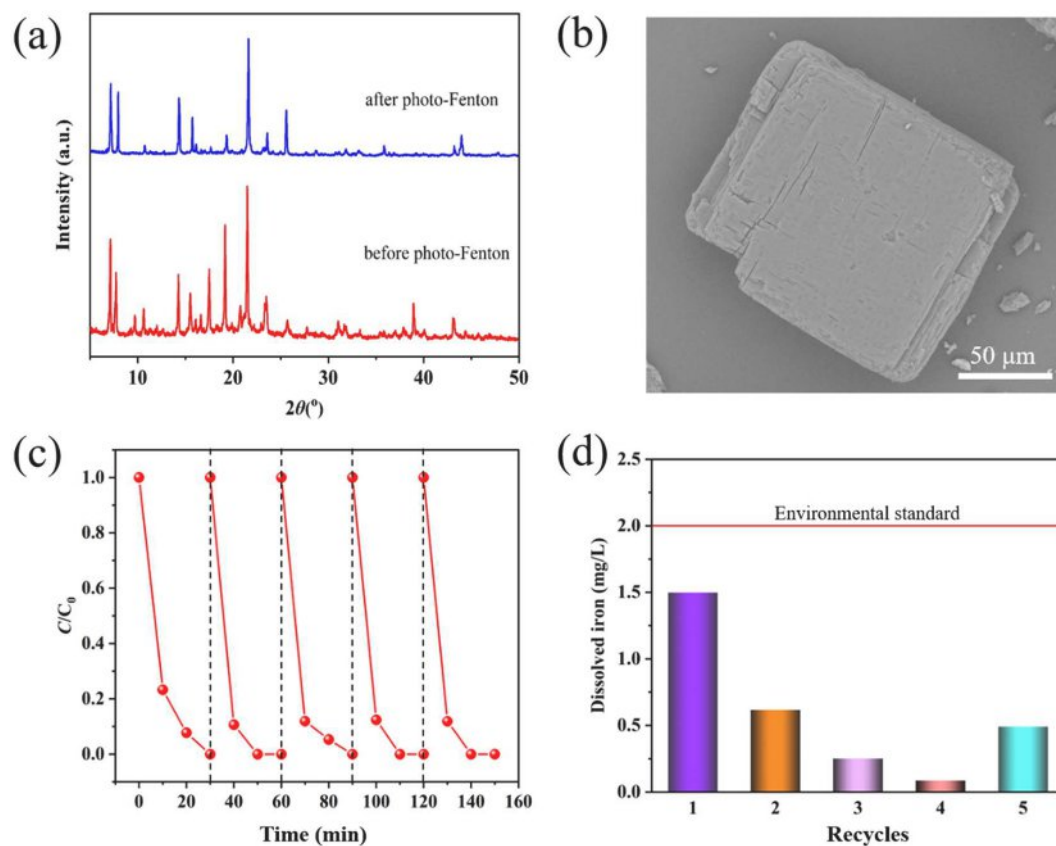
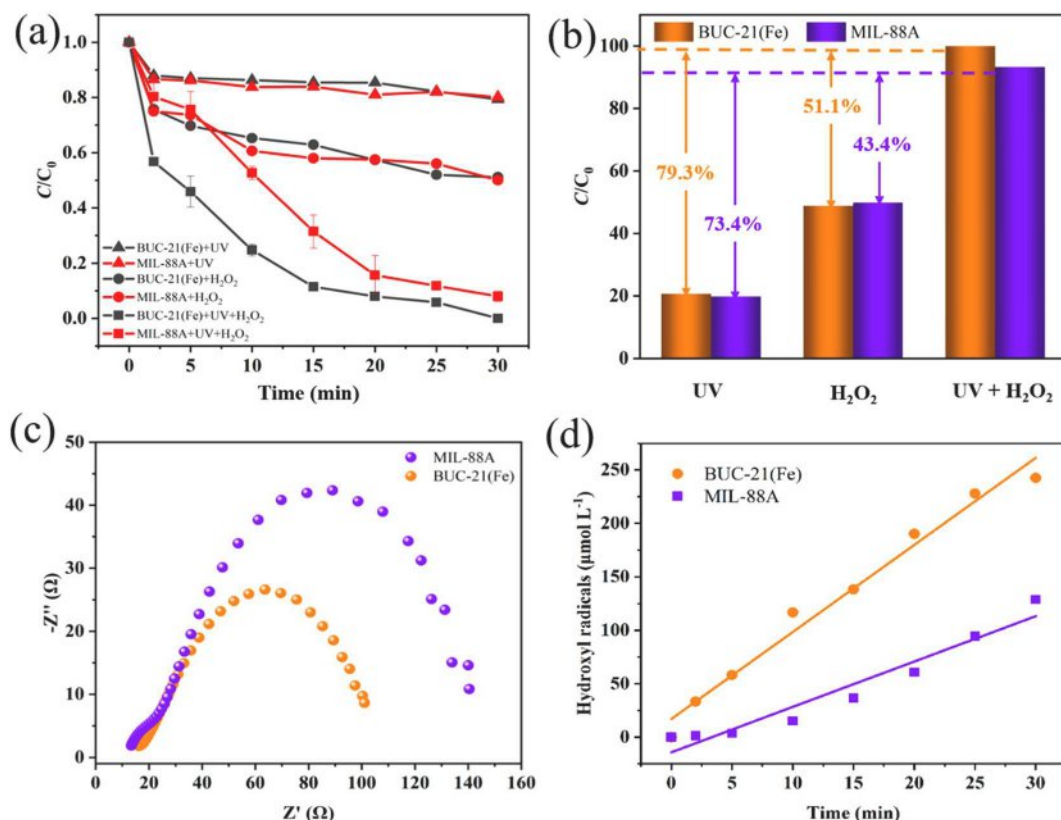
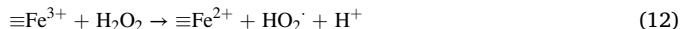


Fig. 11. (a) PXRD patterns of BUC-21(Fe) before and after photo-Fenton reaction; (b) SEM image of BUC-21(Fe) after photo-Fenton reaction; (c) Reusability of BUC-21(Fe) in five consecutive runs and (d) leaching iron ion after per run in photo-Fenton CQ degradation system.





**Fig. 12.** (a) Degradation and (b) removal efficiencies of CQ over BUC-21(Fe) and MIL-88A under different conditions; (c) Nyquist plot of BUC-21(Fe) and MIL-88A; (d) Concentration of ·OH radicals with time over BUC-21(Fe) and MIL-88A. Reaction conditions: 15 mg catalyst, 15  $\mu\text{L}$  H<sub>2</sub>O<sub>2</sub>, 50 mL CQ (10 mg L<sup>-1</sup>), pH = 5.0, 10 W LED UV light (365 nm).



### 3.6. Possible CQ degradation pathway and toxicity assessment of its intermediates

In our previous report, DFT calculation was used to clarify the sites of CQ molecule where were greater tendency for ROS attack in photocatalysis-activated sulfate radical-advanced oxidation process (SR-AOP) over MIL-88A composites [8]. The Fukui indexes of CQ molecule on nucleophilic ( $f^+$ ) and electrophilic attack ( $f^-$ ) were illustrated in Fig. S9. It is widely considered that ·OH is non-selectivity. Therefore, the sites with higher Fukui indexes like the C1 ( $f^- = 0.0914$ ), C2 ( $f^+ = 0.1131$ ), C5 ( $f^+ = 0.0729$ ), C8 ( $f^+ = 0.1306$ ), C9 ( $f^+ = 0.1273$ ), N15 ( $f^- = 0.1094$ ), N17 ( $f^- = 0.1145$ ) and N34 ( $f^- = 0.1487$ ), are inclined to be attacked by ·OH radicals. The intermediates of CQ during the oxidation process were detected by UPLC-MS. Based on DFT calculation and UPLC-MS products identification, the CQ degradation pathway was proposed and depicted in Fig. 9. The N15-C4 cleavage and oxidation to form product B ( $m/z = 322$ ), which was hydroxylated to be product C ( $m/z = 340$ ) quickly [73] (Route 1). The N17 and N34 on the side chain is easy to be attacked, similar with that in sulfate radical-advanced

oxidation process [8]. The product D ( $m/z = 114$ ) and product E ( $m/z = 159$ ) were detected, which produced from the broken of N17-C19 bond or N17-C2 bond (Route 2: A  $\rightarrow$  E  $\rightarrow$  F). The aromatic intermediates were further oxidative ring open and form small molecule (product M). Finally, the intermediates could be completely mineralized into CO<sub>2</sub>. It was found that 16.7% removal efficiency of the total organic carbon (TOC) was accomplished within 30 min.

The toxicity, including bioaccumulation factor, growth inhibition, *Daphnia magna* LC<sub>50</sub> and mutagenicity of CQ and the degradation products were assessed by Toxicity Estimation Software (T.E.S.T.) according to the quantitative structure-activity relationship (QSAR) prediction [8,74]. As displayed in Fig. 10, the bioaccumulation factors of products were obviously decreased. The 48 h *T. pyriformis* IGC<sub>50</sub> of the product B, C and I were still toxic (<10 mg L<sup>-1</sup>), whereas for the further oxidation products, the toxicity was significant declined to not harmful (>100 mg L<sup>-1</sup>) since the broken of benzene ring. The CQ with a *Daphnia magna* LC<sub>50</sub> value of 2.9 mg L<sup>-1</sup> was considered toxicity, while the values of products (like product G, J and C) were decreased to above 10 mg L<sup>-1</sup> (harmful) and even to > 1000 mg L<sup>-1</sup> (not harmful) for product M. The degradation process also decreased the mutagenicity of CQ, besides product M. The results of toxicity assessment suggested that the photo-Fenton process could decrease the comprehensive toxicity of the CQ.

### 3.7. Stability and reusability of BUC-21(Fe)

The stability of MOFs is important, since the structure not only suffer from water, but also being attacked by ROS during the whole AOPs. It was believed that MOFs based on “hard” metals (e.g. Zr and Fe) linked by organic carboxylate ligands own high stability in water [11]. Ye et al. demonstrated that the oxidative resistance and strong affinity of pyridine ring with Fe could greatly enhance the water stability of MOF [35]. Therefore, BUC-21(Fe), Fe nodes and linked by an organic carboxylate

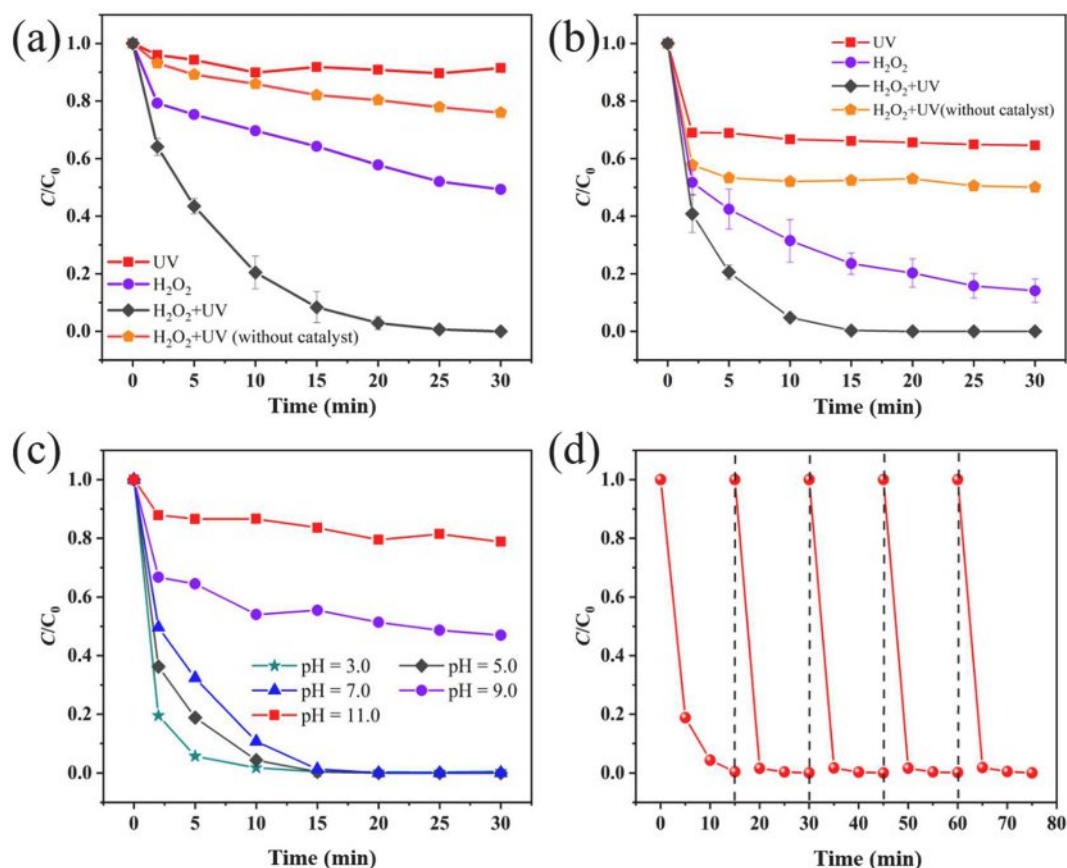


**Fig. 13.** Degradation of (a) SMX and (b) BPA under different conditions; (c) Effect of pH on BPA degradation; (d) The cyclic experiment of photo-Fenton degradation of BPA. Reaction conditions: 15 mg BUC-21(Fe), 50 mL SMX ( $5 \text{ mg L}^{-1}$ ) with 15  $\mu\text{L}$   $H_2O_2$  or BPA ( $10 \text{ mg L}^{-1}$ ) with 10  $\mu\text{L}$   $H_2O_2$ , UV light.

ligand and a rigid ligand with pyridine ring, is considered to be stable during the photo-Fenton reaction. As showed in Fig. 11a, the XRD pattern of BUC-21(Fe) after photo-Fenton reaction was fitted well with that of the fresh sample. Besides, the morphology experienced no obvious change (Fig. 11b), indicating that the structure of BUC-21(Fe) was stable.

The reusability of BUC-21(Fe) was evaluated from CQ degradation for five runs. As showed in Fig. 11c, almost complete CQ was degraded even after fifth run, suggesting good reusability of the catalyst. The

concentration of Fe ion leaching from the catalyst was no  $>1.5 \text{ mg L}^{-1}$  at each run (Fig. 11d), less than that of the environmental standard ( $2 \text{ mg L}^{-1}$ ) [75], further confirming good stability of BUC-21(Fe) during photo-Fenton reaction.

### 3.8. Comparison of the photo-Fenton activities between BUC-21(Fe) and MIL-88A

MIL-88A is a 3D Fe-MOF owing excellent light absorption perfor-

**Table 1**

Comparison of photo-Fenton degradation activities toward the SMX and BPA over different Fe based catalysts.

Catalyst	Organic pollutant	$C_0$ (mg $\text{L}^{-1}$ )	Catalyst dosage (mg)	$H_2O_2$ dosage (mmol $\text{L}^{-1}$ )	pH	Light source	Time (min)	Removal efficiency (%)	Ref.
MIL-88B-Fe/ $\text{Ti}_3\text{C}_2$	SMX	30	10	10	3	500 W, vis	120	99	[77]
NiFe-CNT	SMX	5	1	7.84	5	100 W, UV	120	100	[78]
$\text{CuFe}_2\text{O}_4$	SMX	10	20	10	6.7	300 W, vis	120	96	[79]
MIL-88A	SMX	5	15	2.94	5	10 W, UV	30	52	This work
MIL-101(Fe)	SMX	5	15	2.94	5	10 W, UV	30	50	This work
BUC-21(Fe)	SMX	5	15	2.94	5	10 W, UV	25	100	This work
PANI/MIL-88A (Fe)	BPA	10	10	3.92	/	5 W, white light	30	100	[38]
$\text{Fe}^0$ -vermiculite	BPA	91	50	20	5	300 W, vis	120	94	[80]
MIL-88(A)	BPA	10	10	19.6	/	10 W, vis	60	100	[37]
MIL-101(Fe)	BPA	10	15	2.94	5	10 W, UV	30	98	This work
BUC-21(Fe)	BPA	10	15	2.94	5	10 W, UV	15	100	This work

Note: CNT = carbon nanotube; PANI = Polyaniline.

mance from UV to visible light, similar with that of BUC-21(Fe). Many studies have proved that MIL-88A is a potential photocatalyst for photo-Fenton process [36,38,76]. In order to better understand the advantage of BUC-21(Fe), MIL-88A was selected to degrade CQ under the same conditions. As described in Fig. 12a–12b, the CQ removal efficiencies over BUC-21(Fe) were identical to that over MIL-88A in photocatalysis system (catalyst + UV) and heterogenous Fenton systems (catalyst + H<sub>2</sub>O<sub>2</sub>), respectively. However, in photo-Fenton process (catalyst + H<sub>2</sub>O<sub>2</sub> + UV), 93.3% CQ was decomposed over MIL-88A with TOF 0.3153 L g<sup>-1</sup> min<sup>-1</sup>, whereas 100% CQ was degraded over BUC-21(Fe) with higher TOF (0.3873 L g<sup>-1</sup> min<sup>-1</sup>) within 30 min. As showed in Fig. 12c, the radius of circular arc of BUC-21(Fe) in electrochemical impedance spectroscopy (EIS) Nyquist plots was smaller than that of MIL-88A, indicating smaller charge transfer resistance and higher separate efficiency of the electron-hole pairs on BUC-21(Fe). Besides, the generated ·OH was qualitatively analyzed by UPLC. Under the same conditions, the ·OH concentration generated over BUC-21(Fe) was 242.5 μmol L<sup>-1</sup> (Fig. 12d), nearly 1.9 times as high as that over MIL-88A (128.6 μmol L<sup>-1</sup>). Moreover, the conversion efficiencies from H<sub>2</sub>O<sub>2</sub> to ·OH over BUC-21(Fe) and MIL-88A were calculated by the Eq. (13), where *M*, *m*<sub>1</sub> and *m*<sub>2</sub> is the mass of the generated ·OH (mol), the dosage of catalyst (g) and the volume of H<sub>2</sub>O<sub>2</sub> (L), respectively. The *n*<sub>·OH</sub> values were calculated to be 179.6 and 95.3 mol g<sup>-1</sup> L<sup>-1</sup> for BUC-21(Fe) and MIL-88A, respectively. The results confirmed that BUC-21(Fe) exhibited better performance for decomposing H<sub>2</sub>O<sub>2</sub> to form ·OH than MIL-88A.

$$n_{\cdot\text{OH}} = \frac{M}{m_1 \times m_2} \quad (13)$$

### 3.9. The universality toward other emerging organic pollutants in the photo-Fenton process over BUC-21(Fe)

In order to further explore the photo-Fenton performance of BUC-21(Fe), degradation of some other organic pollutants like SMX and BPA were carried out under similar conditions. The results showed that both SMX and BPA could be completely removed within 25 and 15 min (Fig. 13a–b and Fig. S10), respectively, suggesting excellent universality of BUC-21(Fe). The influences of initial pH on photo-Fenton degradation efficiency were also studied, which suggested that the pollutants could be efficiently removed at a range pH of 3.0–7.0 (Fig. 13c and Fig. S11). As well, five reuse cycles of BUC-21(Fe) for photo-Fenton BPA degradation was explored, which demonstrated that the removal efficiency of BPA kept at a high level (~100%) at each run (Fig. 13d). The results re-confirmed the good reusability of BUC-21(Fe). BUC-21(Fe) exhibited superior photo-Fenton performance toward organic pollutants degradation to the counterpart Fe-based catalysts (Table 1).

## 4. Conclusion

A micron-sized 2D MOF BUC-21(Fe) sheet was synthesized, which displayed excellent heterogeneous photo-Fenton activity and high stability in water. CQ, as emerging organic pollutant model, was degraded efficiently within 30 min at pH = 5.0. The high efficiency might be contributed to the following: (i) Fast mass transport rate (H<sub>2</sub>O<sub>2</sub> and organic pollutants) and easy accessibility of the active sites because of the unique 2D structure; (ii) The inhibited recombination of electron and hole due to the photo-excited electron being consumed by H<sub>2</sub>O<sub>2</sub> and Fe<sup>3+</sup>; (iii) H<sub>2</sub>O<sub>2</sub> being decomposed to form ·OH with high yield efficiency of 242.5 μmol L<sup>-1</sup> by both Fe<sup>2+</sup> and photo-excited electron; (iv) Fe<sup>3+</sup> being reduced to Fe<sup>2+</sup> via the reaction between H<sub>2</sub>O<sub>2</sub> and photo-excited electron to achieve efficient generation of Fe<sup>2+</sup>. It was observed that CQ was degraded into small molecules via heterogeneous photo-Fenton reaction, in which the comprehensive toxicity of the system was greatly reduced. Besides CQ, some other emerging organic pollutants like SMX and BPA can also be decomposed effectively over BUC-21(Fe) sheets via photo-Fenton-like reaction, indicating that BUC-

21(Fe) can be adopted to degrade general organic pollutants without selectivity. This work might tap a door that micron-sized 2D MOFs sheets may be potential candidates for heterogeneous photo-Fenton process.

## CRediT authorship contribution statement

**Fu-Xue Wang:** Data curation, Investigation, Visualization, Writing – original draft. **Chong-Chen Wang:** Conceptualization, Funding acquisition, Supervision, Project administration, Writing – review & editing. **Xuedong Du:** Methodology, Validation. **Yang Li:** Resources, Software. **Fei Wang:** Data curation, Investigation. **Peng Wang:** Resources.

## Declaration of Competing Interest

The authors declare that they have no known competing financial interests or personal relationships that could have appeared to influence the work reported in this paper.

## Acknowledgements

This work was supported by National Natural Science Foundation of China (51878023, 22176012), Beijing Natural Science Foundation (8202016), Great Wall Scholars Training Program Project of Beijing Municipality Universities (CIT&TCD20180323), Beijing Talent Project (2020A27) and The Fundamental Research Funds for Beijing University of Civil Engineering and Architecture (X20147/X20141/X20135/X20146).

## Appendix A. Supplementary data

Supplementary data to this article can be found online at <https://doi.org/10.1016/j.cej.2021.132495>.

## References

- [1] H. Huang, T. Guo, K. Wang, Y. Li, G. Zhang, Efficient activation of persulfate by a magnetic recyclable rape straw biochar catalyst for the degradation of tetracycline hydrochloride in water, *Sci. Total Environ.* 758 (2021), 143957.
- [2] Z. Li, X. Xu, X. Sheng, P. Lin, J. Tang, L. Pan, Y.V. Kaneti, T. Yang, Y. Yamauchi, Solar-powered sustainable water production: state-of-the-art technologies for sunlight–energy–water nexus, *ACS Nano* 15 (2021) 12535–12566.
- [3] Z. Wang, L. Jiang, K. Wang, Y. Li, G. Zhang, Novel AgI/BiSbO<sub>4</sub> heterojunction for efficient photocatalytic degradation of organic pollutants under visible light: interfacial electron transfer pathway, DFT calculation and degradation mechanism study, *J. Hazard. Mater.* 410 (2021), 124948.
- [4] Z. Wang, K. Wang, Y. Li, L. Jiang, G. Zhang, Novel BiSbO<sub>4</sub>/BiOBr nanoarchitecture with enhanced visible-light driven photocatalytic performance: oxygen-induced pathway of activation and mechanism unveiling, *Appl. Surf. Sci.* 498 (2019), 143850.
- [5] J. Guo, L. Wang, X. Wei, Z.A. Allothman, M.D. Albaqami, V. Malgras, Y. Yamauchi, Y. Kang, M. Wang, W. Guan, X. Xu, Direct Z-scheme CuInS<sub>2</sub>/Bi<sub>2</sub>MoO<sub>6</sub> heterostructure for enhanced photocatalytic degradation of tetracycline under visible light, *J. Hazard. Mater.* 415 (2021), 125591.
- [6] Z. Zhuge, X. Liu, T. Chen, Y. Gong, C. Li, L. Niu, S. Xu, X. Xu, Z.A. Allothman, C. Q. Sun, J.G. Shapter, Y. Yamauchi, Highly efficient photocatalytic degradation of different hazardous contaminants by CaIn<sub>2</sub>S<sub>4</sub>-Ti<sub>3</sub>C<sub>2</sub>Tx Schottky heterojunction: an experimental and mechanism study, *Chem. Eng. J.* 421 (2021), 127838.
- [7] T. Guo, L. Jiang, K. Wang, Y. Li, H. Huang, X. Wu, G. Zhang, Efficient persulfate activation by hematite nanocrystals for degradation of organic pollutants under visible light irradiation: facet-dependent catalytic performance and degradation mechanism, *Appl. Catal. B* 286 (2021), 119883.
- [8] X.-H. Yi, H. Ji, C.-C. Wang, Y. Li, Y.-H. Li, C. Zhao, A. Wang, H. Fu, P. Wang, X. Zhao, W. Liu, Photocatalysis-activated SR-AOP over PDINH/MIL-88A(Fe) composites for boosted chloroquine phosphate degradation: performance, mechanism, pathway and DFT calculations, *Appl. Catal. B* 293 (2021), 120229.
- [9] J. Ji, Q. Yan, P. Yin, S. Mine, M. Matsuoka, M. Xing, Defects on CoS<sub>2</sub>–x: tuning redox reactions for sustainable degradation of organic pollutants, *Angew. Chem.* 60 (2021) 2903–2908.
- [10] Q. Yan, C. Lian, K. Huang, L. Liang, H. Yu, P. Yin, J. Zhang, M. Xing, Constructing an acidic microenvironment by MoS<sub>2</sub> in heterogeneous fenton reaction for pollutant control, *Angew. Chem. Int. Ed.* 60 (2021) 17155–17163.
- [11] C.-C. Wang, J.-R. Li, X.-L. Lv, Y.-Q. Zhang, G. Guo, Photocatalytic organic pollutants degradation in metal–organic frameworks, *Energy Environ. Sci.* 7 (9) (2014) 2831–2867.



- [12] Y. Zhu, R. Zhu, Y. Xi, J. Zhu, G. Zhu, H. He, Strategies for enhancing the heterogeneous Fenton catalytic reactivity: a review, *Appl. Catal. B* 255 (2019) 117739, <https://doi.org/10.1016/j.apcatb.2019.05.041>.
- [13] X. Hou, X. Huang, F. Jia, Z. Ai, J. Zhao, L. Zhang, Hydroxylamine promoted goethite surface fenton degradation of organic pollutants, *Environ. Sci. Technol.* 51 (9) (2017) 5118–5126.
- [14] R. Zhu, Y. Zhu, H. Xian, L. Yan, H. Fu, G. Zhu, Y. Xi, J. Zhu, H. He, CNTs/ferrihydrite as a highly efficient heterogeneous Fenton catalyst for the degradation of bisphenol A: the important role of CNTs in accelerating Fe(III)/Fe(II) cycling, *Appl. Catal. B* 270 (2020) 118891, <https://doi.org/10.1016/j.apcatb.2020.118891>.
- [15] Y. Ju, Y. Yu, X. Wang, M. Xiang, L. Li, D. Deng, D.D. Dionysiou, Environmental application of millimetre-scale sponge iron (s-FeO) particles (IV): new insights into visible light photo-Fenton-like process with optimum dosage of H<sub>2</sub>O<sub>2</sub> and RhB photosensitizers, *J. Hazard. Mater.* 323 (2017) 611–620.
- [16] G. Ren, M. Zhou, M. Liu, L. Ma, H. Yang, A novel vertical-flow electro-Fenton reactor for organic wastewater treatment, *Chem. Eng. J.* 298 (2016) 55–67.
- [17] T. Zhou, X. Lu, T.-T. Lim, Y. Li, F.-S. Wong, Degradation of chlorophenols (CPs) in an ultrasound-irradiated Fenton-like system at ambient circumstance: the QSPR (quantitative structure–property relationship) study, *Chem. Eng. J.* 156 (2010) 347–352.
- [18] R.G. Zepp, B.C. Faust, J. Hoigne, Hydroxyl radical formation in aqueous reactions (pH 3–8) of iron(II) with hydrogen peroxide: the photo-Fenton reaction, *Environ. Sci. Technol.* 26 (1992) 313–319.
- [19] X. Wang, X. Zhang, Y.i. Zhang, Y. Wang, S.-P. Sun, W.D. Wu, Z. Wu, Nanostructured semiconductor supported iron catalysts for heterogeneous photo-Fenton oxidation: a review, *J. Mater. Chem. A* 8 (31) (2020) 15513–15546.
- [20] W. Huang, M. Brigante, F. Wu, C. Mousty, K. Hanna, G. Mailhot, Assessment of the Fe(III)-EDDS complex in fenton-like processes: from the radical formation to the degradation of bisphenol A, *Environ. Sci. Technol.* 47 (2013) 1952–1959.
- [21] M. Xing, W. Xu, C. Dong, Y. Bai, J. Zeng, Y.i. Zhou, J. Zhang, Y. Yin, Metal sulfides as excellent co-catalysts for H<sub>2</sub>O<sub>2</sub> decomposition in advanced oxidation processes, *Chem. A* 6 (2018) 1359–1372.
- [22] C. Dong, J. Ji, B. Shen, M. Xing, J. Zhang, Enhancement of H<sub>2</sub>O<sub>2</sub> decomposition by the co-catalytic effect of WS<sub>2</sub> on the Fenton reaction for the synchronous reduction of Cr(VI) and remediation of phenol, *Environ. Sci. Technol.* 52 (19) (2018) 11297–11308.
- [23] J.-R. Li, R.J. Kuppler, H.-C. Zhou, Selective gas adsorption and separation in metal-organic frameworks, *Chem. Soc. Rev.* 38 (5) (2009) 1477, <https://doi.org/10.1039/b802426j>.
- [24] J.-R. Li, H.-C. Zhou, Bridging-ligand-substitution strategy for the preparation of metal-organic polyhedra, *Nat. Chem.* 2 (10) (2010) 893–898.
- [25] B.A. Johnson, A.M. Beiler, B.D. McCarthy, S. Ott, Transport phenomena: challenges and opportunities for molecular catalysis in metal-organic frameworks, *J. Am. Chem. Soc.* 142 (28) (2020) 11941–11956.
- [26] Y. Wen, J. Zhang, Q. Xu, X.-T. Wu, Q.-L. Zhu, Pore surface engineering of metal-organic frameworks for heterogeneous catalysis, *Coord. Chem. Rev.* 376 (2018) 248–276.
- [27] C.-C. Wang, X.-D. Du, J. Li, X.-X. Guo, P. Wang, J. Zhang, Photocatalytic Cr(VI) reduction in metal-organic frameworks: a mini-review, *Appl. Catal. B* 193 (2016) 198–216.
- [28] D. Pang, C.-C. Wang, P. Wang, W. Liu, H. Fu, C. Zhao, Superior removal of inorganic and organic arsenic pollutants from water with MIL-88A(Fe) decorated on cotton fibers, *Chemosphere* 254 (2020), 126829.
- [29] R.J. Kuppler, D.J. Timmons, Q.-R. Fang, J.-R. Li, T.A. Makal, M.D. Young, D. Yuan, D. Zhao, W. Zhuang, H.-C. Zhou, Potential applications of metal-organic frameworks, *Coord. Chem. Rev.* 253 (2009) 3042–3066.
- [30] N.L. Rosi, J. Eckert, M. Eddaoudi, D.T. Vodak, J. Kim, M. Keefe, O.M. Yaghi, Hydrogen storage in microporous metal-organic frameworks, *Science* 300 (2003) 1127.
- [31] J. Guo, X. Xu, J.P. Hill, L. Wang, J. Dang, Y. Kang, Y. Li, W. Guan, Y. Yamauchi, Graphene-carbon 2D heterostructures with hierarchically-porous P, N-doped layered architecture for capacitive deionization, *Chem. Sci.* 12 (2021) 10334–10340.
- [32] Y. Zhao, L. Zheng, D. Jiang, W. Xia, X. Xu, Y. Yamauchi, J. Ge, J. Tang, Nanoengineering metal-organic framework-based materials for use in electrochemical CO<sub>2</sub> reduction reactions, *Small* 17 (2021) 2006590.
- [33] J.-W. Wang, F.-G. Qiu, P. Wang, C. Ge, C.-C. Wang, Boosted bisphenol A and Cr(VI) clean-up over Z-scheme WO<sub>3</sub>/MIL-100(Fe) composites under visible light, *J. Cleaner Prod.* 279 (2021), 123408.
- [34] X. Du, W. Fu, P. Su, J. Cai, M. Zhou, Internal-micro-electrolysis-enhanced heterogeneous electro-Fenton process catalyzed by Fe/Fe<sub>3</sub>C@PC core-shell hybrid for sulfamethazine degradation, *Chem. Eng. J.* 398 (2020), 125681.
- [35] Z. Ye, G.E.M. Schukraft, A. L'Hermite, Y. Xiong, E. Brillas, C. Petit, I. Sirés, Mechanism and stability of an Fe-based 2D MOF during the photoelectro-Fenton treatment of organic micropollutants under UVA and visible light irradiation, *Water Res.* 184 (2020), 115986.
- [36] X. Liao, F. Wang, F. Wang, Y.i. Cai, Y. Yao, B.-T. Teng, Q. Hao, L.u. Shuxiang, Synthesis of (100) surface oriented MIL-88A-Fe with rod-like structure and its enhanced fenton-like performance for phenol removal, *Appl. Catal. B* 259 (2019) 118064, <https://doi.org/10.1016/j.apcatb.2019.118064>.
- [37] H. Fu, X.-X. Song, L. Wu, C. Zhao, P. Wang, C.-C. Wang, Room-temperature preparation of MIL-88A as a heterogeneous photo-Fenton catalyst for degradation of rhodamine B and bisphenol A under visible light, *Mater. Res. Bull.* 125 (2020) 110806, <https://doi.org/10.1016/j.materresbull.2020.110806>.
- [38] D.-D. Chen, X.-H. Yi, L.i. Ling, C.-C. Wang, P. Wang, Photocatalytic Cr(VI) sequestration and photo-Fenton bisphenol A decomposition over white light responsive PANI/MIL-88A(Fe), *Appl. Organomet. Chem.* 34 (9) (2020), <https://doi.org/10.1002/aoc.v34.910.1002/aoc.5795>.
- [39] A. Dhakshinamoorthy, A.M. Asiri, H. Garcia, 2D metal-organic frameworks as multifunctional materials in heterogeneous catalysis and electro/photocatalysis, *Adv. Mater.* 31 (41) (2019) 1900617, <https://doi.org/10.1002/adma.v31.4110.1002/adma.201900617>.
- [40] W. Bai, S. Li, J. Ma, W. Cao, J. Zheng, Ultrathin 2D metal-organic framework (nanosheets and nanofilms)-based xD-2D hybrid nanostructures as biomimetic enzymes and supercapacitors, *J. Mater. Chem. A* 7 (15) (2019) 9086–9098.
- [41] A. Çiftlik, T. Günay Semerci, O. Şahin, F. Semerci, Two-dimensional metal-organic framework nanostructures based on 4,4'-sulfonyldibenzoate for photocatalytic degradation of organic dyes, *Cryst. Growth Des.* 21 (2021) 3364–3374.
- [42] Y. Zhao, J. Wang, R. Pei, Micron-sized ultrathin metal-organic framework sheet, *J. Am. Chem. Soc.* 142 (2020) 10331–10336.
- [43] X. Ding, H. Liu, J. Chen, M. Wen, G. Li, T. An, H. Zhao, In situ growth of well-aligned Ni-MOF nanosheets on nickel foam for enhanced photocatalytic degradation of typical volatile organic compounds, *Nanoscale* 12 (2020) 9462–9470.
- [44] Y. Xiao, X. Guo, T. Yang, J. Liu, X. Liu, Y. Xiao, L. Liu, T. Liu, S. Ye, J. Jiang, F. Zhang, C. Li, Water-stable Mn-based MOF nanosheet as robust visible-light-responsive photocatalyst in aqueous solution, *Science China, Chemistry* 63 (2020) 1756–1760.
- [45] Y. Pan, R. Abazari, J. Yao, J. Gao, Recent progress in 2D metal-organic framework photocatalysts: synthesis, photocatalytic mechanism and applications, *Journal of Physics: Energy* 3 (2021), 032010.
- [46] V. Gosu, B.R. Gurjar, T.C. Zhang, R.Y. Surampalli, Oxidative degradation of quinoline using nanoscale zero-valent iron supported by granular activated carbon, *J. Environ. Eng.* 142 (1) (2016) 04015047, [https://doi.org/10.1061/\(ASCE\)EE.1943-7870.0000981](https://doi.org/10.1061/(ASCE)EE.1943-7870.0000981).
- [47] M. Ramesh, S. Anitha, R.K. Poopal, C. Shobana, Evaluation of acute and sublethal effects of chloroquine (C18H26ClN3) on certain enzymological and histopathological biomarker responses of a freshwater fish *Cyprinus carpio*, *Toxicol. Rep.* 5 (2018) 18–27.
- [48] C. Rendal, K.O. Kusk, S. Trapp, The effect of pH on the uptake and toxicity of the bivalent weak base chloroquine tested on *Salix viminalis* and *Daphnia magna*, *Environ. Toxicol. Chem.* 30 (2) (2011) 354–359.
- [49] F.-X. Wang, X.-H. Yi, C.-C. Wang, J.-G. Deng, Photocatalytic Cr(VI) reduction and organic-pollutant degradation in a stable 2D coordination polymer, *Chin. J. Catal.* 38 (12) (2017) 2141–2149.
- [50] K. Kosaka, H. Yamada, S. Matsui, S. Echigo, K. Shishida, Comparison among the methods for hydrogen peroxide measurements to evaluate advanced oxidation processes: application of a spectrophotometric method using copper(II) ion and 2,9-Dimethyl-1,10-phenanthroline, *Environ. Sci. Technol.* 32 (1998) 3821–3824.
- [51] Y. Zhang, J. Zhou, X. Chen, L. Wang, W. Cai, Coupling of heterogeneous advanced oxidation processes and photocatalysis in efficient degradation of tetracycline hydrochloride by Fe-based MOFs: Synergistic effect and degradation pathway, *Chem. Eng. J.* 369 (2019) 745–757.
- [52] A. Dhakshinamoorthy, M. Alvaro, H. Garcia, Aerobic oxidation of cycloalkenes catalyzed by iron metal organic framework containing N-hydroxyphthalimide, *J. Catal.* 289 (2012) 259–265.
- [53] H. Jia, W. He, B. Zhang, L. Yao, X. Yang, Z. Zheng, Facile synthesis of bismuth oxyhalide nanosheet films with distinct conduction type and photo-induced charge carrier behavior, *Appl. Surf. Sci.* 441 (2018) 832–840.
- [54] X.-H. Yi, S.-Q. Ma, X.-D. Du, C. Zhao, H. Fu, P. Wang, C.-C. Wang, The facile fabrication of 2D/3D Z-scheme g-C<sub>3</sub>N<sub>4</sub>/UiO-66 heterojunction with enhanced photocatalytic Cr(VI) reduction performance under white light, *Chem. Eng. J.* 375 (2019) 121944, <https://doi.org/10.1016/j.cej.2019.121944>.
- [55] J. Liu, X. Zhang, Q. Zhong, J. Li, H. Wu, B.o. Zhang, L. Jin, H.B. Tao, B. Liu, Electrostatic self-assembly of a AgI/Bi<sub>2</sub>Ge<sub>4</sub>O<sub>9</sub> p-n junction photocatalyst for boosting superoxide radical generation, *J. Mater. Chem. A* 8 (7) (2020) 4083–4090.
- [56] L. Sun, R. Li, W. Zhan, Y. Yuan, X. Wang, X. Han, Y. Zhao, Double-shelled hollow rods assembled from nitrogen/sulfur-codoped carbon coated indium oxide nanoparticles as excellent photocatalysts, *Nat. Commun.* 10 (2019) 2270.
- [57] L. Xu, J. Wang, A heterogeneous Fenton-like system with nanoparticulate zero-valent iron for removal of 4-chloro-3-methyl phenol, *J. Hazard. Mater.* 186 (2011) 256–264.
- [58] M. Cheng, C. Lai, Y. Liu, G. Zeng, D. Huang, C. Zhang, L. Qin, L. Hu, C. Zhou, W. Xiong, Metal-organic frameworks for highly efficient heterogeneous Fenton-like catalysis, *Coord. Chem. Rev.* 368 (2018) 80–92.
- [59] Y. Zhu, R. Zhu, Y. Xi, T. Xu, L. Yan, J. Zhu, G. Zhu, H. He, Heterogeneous photo-Fenton degradation of bisphenol A over Ag/AgCl/ferrihydrite catalysts under visible light, *Chem. Eng. J.* 346 (2018) 567–577.
- [60] S. Zhang, X. Zhao, H. Niu, Y. Shi, Y. Cai, G. Jiang, Superparamagnetic Fe<sub>3</sub>O<sub>4</sub> nanoparticles as catalysts for the catalytic oxidation of phenolic and aniline compounds, *J. Hazard. Mater.* 167 (2009) 560–566.
- [61] L. Yang, J. He, Y. Liu, J. Wang, L. Jiang, G. Wang, Characteristics of change in water quality along reclaimed water intake area of the Chaobai River in Beijing, *China, J. Environ. Sci.* 50 (2016) 93–102.
- [62] M. Peters, Q. Guo, H. Strauss, R. Wei, S. Li, F. Yue, Contamination patterns in river water from rural Beijing: a hydrochemical and multiple stable isotope study, *Sci. Total Environ.* 654 (2019) 226–236.



- [63] V.W. Cope, S.-N. Chen, M.Z. Hoffman, Intermediates in the photochemistry of of carbonato-amine complexes of cobalt(III). Carbonate(-) radicals and the aquocarbonato complex, *J. Am. Chem. Soc.* 95 (1973) 3116–3121.
- [64] V.K. Sharma, M. Feng, Water depollution using metal-organic frameworks-catalyzed advanced oxidation processes: a review, *J. Hazard. Mater.* 372 (2019) 3–16.
- [65] J. Cai, M. Zhou, Y. Pan, X. Du, X. Lu, Extremely efficient electrochemical degradation of organic pollutants with co-generation of hydroxyl and sulfate radicals on Blue-TiO<sub>2</sub> nanotubes anode, *Appl. Catal. B* 257 (2019), 117902.
- [66] D. Yu, L. Li, M. Wu, J.C. Crittenden, Enhanced photocatalytic ozonation of organic pollutants using an iron-based metal-organic framework, *Appl. Catal. B* 251 (2019) 66–75.
- [67] X. Yang, J. He, Z. Sun, A. Holmgren, D. Wang, Effect of phosphate on heterogeneous Fenton oxidation of catechol by nano-Fe<sub>3</sub>O<sub>4</sub>: Inhibitor or stabilizer? *J. Environ. Sci.* 39 (2016) 69–76.
- [68] A.P. Grosvenor, B.A. Kobe, M.C. Biesinger, N.S. McIntyre, Investigation of multiplet splitting of Fe 2p XPS spectra and bonding in iron compounds, *Surf. Interface Anal.* 36 (2004) 1564–1574.
- [69] Q. Chen, J. Li, L. Cheng, H. Liu, Construction of CdLa<sub>2</sub>S<sub>4</sub>/MIL-88A(Fe) heterojunctions for enhanced photocatalytic H<sub>2</sub>-evolution activity via a direct Z-scheme electron transfer, *Chem. Eng. J.* 379 (2020), 122389.
- [70] A. Deb, U. Bergmann, E.J. Cairns, S.P. Cramer, Structural investigations of LiFePO<sub>4</sub> electrodes by Fe X-ray absorption spectroscopy, *J. Phys. Chem. B* 108 (2004) 7046–7051.
- [71] T. Guo, K. Wang, G. Zhang, X. Wu, A novel  $\alpha$ -Fe<sub>2</sub>O<sub>3</sub>@g-C<sub>3</sub>N<sub>4</sub> catalyst: Synthesis derived from Fe-based MOF and its superior photo-Fenton performance, *Appl. Surf. Sci.* 469 (2019) 331–339.
- [72] R. Deng, H. Luo, D. Huang, C. Zhang, Biochar-mediated Fenton-like reaction for the degradation of sulfamethazine: role of environmentally persistent free radicals, *Chemosphere* 255 (2020), 126975.
- [73] C. Wang, K. Ma, T. Wu, M. Ye, P. Tan, K. Yan, Electrochemical mineralization pathway of quinoline by boron-doped diamond anodes, *Chemosphere* 149 (2016) 219–223.
- [74] R. Yin, Y. Chen, S. He, W. Li, L. Zeng, W. Guo, M. Zhu, In situ photoreduction of structural Fe(III) in a metal-organic framework for peroxydisulfate activation and efficient removal of antibiotics in real wastewater, *J. Hazard. Mater.* 388 (2020), 121996.
- [75] M. Ahmad, S. Chen, F. Ye, X. Quan, S. Afzal, H. Yu, X. Zhao, Efficient photo-Fenton activity in mesoporous MIL-100(Fe) decorated with ZnO nanosphere for pollutants degradation, *Appl. Catal. B* 245 (2019) 428–438.
- [76] W.-T. Xu, L. Ma, F. Ke, F.-M. Peng, G.-S. Xu, Y.-H. Shen, J.-F. Zhu, L.-G. Qiu, Y.-P. Yuan, Metal-organic frameworks MIL-88A hexagonal microrods as a new photocatalyst for efficient decolorization of methylene blue dye, *Dalton Trans.* 43 (2014) 3792–3798.
- [77] M. Ahmad, X. Quan, S. Chen, H. Yu, Tuning Lewis acidity of MIL-88B-Fe with mix-valence coordinatively unsaturated iron centers on ultrathin Ti<sub>3</sub>C<sub>2</sub> nanosheets for efficient photo-Fenton reaction, *Appl. Catal. B* 264 (2020), 118534.
- [78] M. Nawaz, A. Shahzad, K. Tahir, J. Kim, M. Moztahida, J. Jang, M.B. Alam, S.-H. Lee, H.-Y. Jung, D.S. Lee, Photo-Fenton reaction for the degradation of sulfamethoxazole using a multi-walled carbon nanotube-NiFe<sub>2</sub>O<sub>4</sub> composite, *Chem. Eng. J.* 382 (2020), 123053.
- [79] J. Gao, S. Wu, Y. Han, F. Tan, Y. Shi, M. Liu, X. Li, 3D mesoporous CuFe<sub>2</sub>O<sub>4</sub> as a catalyst for photo-Fenton removal of sulfonamide antibiotics at near neutral pH, *J. Colloid Interface Sci.* 524 (2018) 409–416.
- [80] S. Yang, P. Wu, Q. Ye, W. Li, M. Chen, N. Zhu, Efficient catalytic degradation of bisphenol A by novel Fe<sub>0</sub>-vermiculite composite in photo-Fenton system: mechanism and effect of iron oxide shell, *Chemosphere* 208 (2018) 335–342.